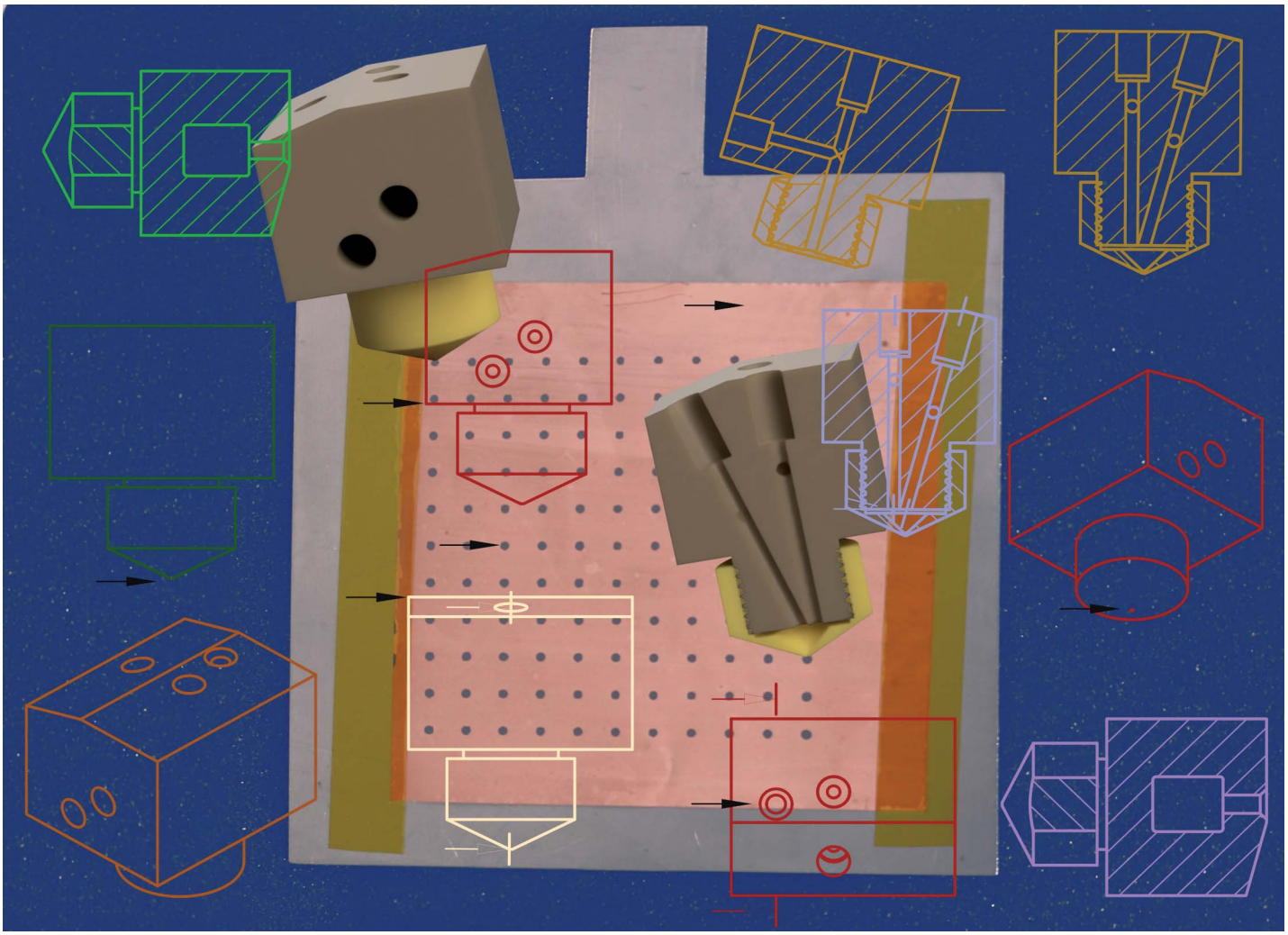

Showcasing research from Fuzhan Rahmanian and Professor Helge Sören Stein from Technical University of Munich, Bavaria, Germany.

Autonomous millimeter scale high throughput battery research system

Millimeter-scale high-throughput battery research (MISCHBARES) on slurry-derived electrodes is herein integrated with data analysis, data management, and quality control for expedited knowledge generation. In-depth high-throughput XPS and XRF enable correlative spectroscopy across all states of charge (SOC). This research is enabled by the hierarchical experimental laboratory automation and orchestration framework (HELAO) and the Modular and Autonomous Data Analysis Platform (MADAP) which offer quality control gates and data lineage tracking.

As featured in:

See Fuzhan Rahmanian, Helge Sören Stein *et al.*, *Digital Discovery*, 2024, **3**, 883.

ROYAL SOCIETY OF CHEMISTRY

rsc.li/digitaldiscovery

Registered charity number: 207890

Digital Discovery

ROYAL SOCIETY OF CHEMISTRY

PAPER

Cite this: *Digital Discovery*, 2024, **3**, 883

Autonomous millimeter scale high throughput battery research system†

Fuzhan Rahmanian, *[abdef] Stefan Fuchs,[ab] Bojing Zhang,[abdef] Maximilian Fichtner [ac] and Helge Sören Stein*[abdef]

Discoveries of novel electrolyte–electrode combinations require comprehensive structure–property–interface correlations. Herein, we present autonomous millimeter scale high-throughput battery research system (Auto-MISCHBARES) operated with an asynchronous web-based orchestration framework that integrates modular research instrumentation designed for autonomous electrochemical experimentation. The platform allows researchers to define a range of experiments with granular parameter control, start the process, and receive a live visualization of measurements through a web-based user interface. This paper presents a proof of concept for cathode electrolyte interphase (CEI) formation in lithium-ion batteries (LiBs) at various potentials, all controlled through Auto-MISCHBARES and correlating its high-throughput electrochemistry results with X-ray photoelectron spectroscopy (XPS) characterization. We believe quality control, complex data analysis, and management to be the missing puzzle pieces toward more complex workflow automation. Auto-MISCHBARES integrates automatic quality control for both hardware and software using AI enablers to ensure high reliability through an on-the-fly fidelity assessment of each experiment. In the presented case study, voltammetry measurements are handled through a modular platform capable of performing fully automated analysis, while data lineage is provided through relational data storage in adherence with Findable, Accessible, Interoperable, and Reusable (FAIR) guidelines, all in real-time. Thus, Auto-MISCHBARES represents a point of contact between the orchestration of automated instrumentation, quality control, real-time data analysis, and management, enabling reproducible and versatile workflows for the discovery of new materials, especially for batteries. We demonstrate this integrated workflow for reliable charging/discharging protocols.

Received 31st December 2023
Accepted 15th March 2024

DOI: 10.1039/d3dd00257h

rsc.li/digitaldiscovery

Automated quality control and data interpretation are the missing puzzle pieces towards prolonged walk-away-times in closed-loop experimentation.[1] These advances increase the efficiency and innovation of the research process by minimizing the need for human oversight and ensuring the generation of reliable, insightful data. Early demonstrations of closed-loop experiments included mostly error resilient measurement and facile data analysis, but the step towards complex and interrelated experimentation necessitates more robust data quality assessment. The evolution of these automated experiments towards truly autonomous Material Acceleration Platforms (MAPs) requires integration of experimental processes, data management, and strategic decision-making[2] self-driving laboratories (SDLs).[3,4] Laboratories such as BEAR,[5] ARES,[6] Clio,[7] equipped with advanced frameworks are instrumental in boosting operational efficiency and research safety.[8] These technological leaps not only streamline experimental processes, but also enable scientists to undertake deeper and more intricate inquiries, accelerating discovery in various scientific domains.[9,10] Additionally, the integration of AI and machine learning (ML) allows for efficient exploration of complex chemical and material terrains.[10,11] SDLs, in particular, show the potential to accelerate research output by up to 30 times.[9] By automating and digitalizing processes, these systems increase experimental accuracy and walk away time.[4]

1 The challenge of multifidelity

There is a sprawl of MAPs in various fields[12–14] but its progress in non-aqueous battery applications has been hindered by unique challenges.[15] As a result, only a few established MAP efforts exist, chief among which is the Battery Interface Genome-Materials

[a]*Helmholtz Institute Ulm, Applied Electrochemistry, Helmholtzstr. 11, 89081 Ulm, Germany*

[b]*Karlsruhe Institute of Technology, Institute of Physical Chemistry, Fritz-Haber-Weg 2, 76131 Karlsruhe, Germany*

[c]*Karlsruhe Institute of Technology, Institute of Nanotechnology, 76021 Karlsruhe, Germany*

[d]*Technische Universität München, School of Natural Sciences, Department of Chemistry, Lichtenbergstr 4, 85748 Garching, Germany. E-mail: helge.stein@tum.de; fuzhan.rahmanian@tum.de*

[e]*Technische Universität München, Munich Data Science Institute, Walther-von-Dyck-Straße 10, 4, 85748 Garching, Germany*

[f]*Technische Universität München, Munich Institute for Robotic and Machine Intelligence, Georg-Brauchle-Ring 60-62, 80992 Munich, Germany*

† Electronic supplementary information (ESI) available. See DOI: https://doi.org/10.1039/d3dd00257h

Acceleration Platform (BIG-MAP) initiative.[16] This complexity arises mainly from the special housing and safety measures necessary to conduct battery research and the vast chemical space required to optimize, for example, electrolytes, electrodes, design, and physical properties.[17–19] Significant efforts have been made to address each aspect; for instance, Dave *et al.*[7] developed an autonomous workflow to optimize the electrolyte formulation for a single salt and ternary solvent design at various ratios for non-aqueous battery systems by utilizing a robotic platform. At the interface level, the autonomous investigation of CEI and solid electrolyte interphase (SEI) within MAPs are not extensively explored on an experimental level.[20–22] This highlights the ongoing need for innovative approaches in battery studies, especially in understanding and optimizing the complex interactions at these interfaces,[23,24] which involve multiple and varied testing scenarios, such as the correlation of electrochemical and spectroscopy characterization. A challenge in developing a system capable of providing a multifaceted solution for the next generation of battery materials[19] is the integration of all the necessary devices within a single laboratory.[25] Herein, granular control across each step of the experimentation is crucial for achieving multifidelity. Additionally, due to variations arising from different samples, experimental correlation and device integration within a single lab become even more critical to ensure consistency and reliability of results, as it effectively minimizes discrepancies that might occur from diverse laboratory environments.

2 The challenge of designing an integrative database solution

To address the challenges of multi-device testing on a single sample, the development of a robust data management is essential.[24,26–28] This system must enable seamless integration and communication across various instruments and bridge physical and temporal gaps in experimental stages that often exist between disparate phases.[29,30] Such advancements are crucial in SDLs, where progress has been hindered by a lack of standardized and user-friendly software between laboratory instrumentation and intuitive operational guidelines.[15] Efficient data management and experimental planning enable rapid processing and interpretation of high dimensional data, which unravel physicochemical relations that surpass the analytical capacity of conventional approaches.[1,31,32] It also facilitates the incorporation of AI agents and Deep Learning (DL) tools, which can further accelerate the exploration of the chemical spaces and reduce recourse allocation.[32–34] This approach is in line with significant scientific efforts in chemistry[35] and in other domains,[10] which emphasize the importance of consistent data quality protocols and data acquisition methods, in compliance with FAIR data principles.[36]

3 AI enablers for reliable experimentation

In autonomous experimental setups, replicating burdensome human-intensive tasks, such as material sufficiency management or equipment cleaning, is challenging.[2,37] Simultaneously, these ensure the reliability and fidelity of measurements and require rigorous validation for experimental accuracy and consideration of potential hardware and software flaws.[38] As proposed in recent studies,[4,39,40] the utilization of AI technology, such as ML and computer vision methods, can significantly improve system robustness, which is crucial to monitor parameter validity in real time.[4] The goal is to achieve data integrity and support AI planners in informed decision-making. This is particularly beneficial for non-aqueous battery systems experimentation in gloveboxes, where assembling and controlling multiple experiments present complexities that even with human intervention may prove challenging to manage effectively. The progress in adopting AI enablers, thus, signifies a transformative shift in scientific experimentation towards enhanced precision and reliability,[39] highlighted by the critical need to recognize and address the technical challenges in experiment-specific boundaries to ensure results are both comprehensible and reproducible.[14,41]

To advance the MAPs and overcome existing constraints of multifidelity, robust data management, and reliable and reproducible automated experimentation,[9,10] we introduce the Auto-MISCHBARES, an open-source framework designed for fully unsupervised operations. Building upon our earlier studies on asynchronous web-based frameworks,[30] it orchestrates live visualization of electrochemical measurements, quality control and user feedback, data provenance and analysis, thus enhancing the experimental processes. This platform features automated capabilities for conducting a variety of electrochemical experiments configured over a web user interface (UI), as showcased in our case study of the CEI formation on screen-printed battery electrodes. Auto-MISCHBARES performed sequential measurements using an open-cell setup[42] and characterized them using XPS under ultra-high vacuum conditions. The agnostic nature of our framework ensures its adaptability for diverse organic and inorganic materials. This platform not only can accelerate research but also facilitate the sharing of validated data, helping scientists in the efficient extraction and transfer of information within the community.[37,43]

4 Design and methodology

4.1 Framework overview

The Auto-MISCHBARES framework is developed by integrating four key Hubs overarching hardware and software of the experimental workflow. The DeviceHub encompasses a set of hardware that is responsible for the exact placement, dispensing, and measurement. The ServerHub ensures robust operations and communication workflow through orchestration and API design. The DataHub manages the database environment and is key for data integrity and accessibility. Lastly, the MultiAnalyticHub provides a wide spectrum of analytics, from statistical assessments to computer vision methods.[46] The integration of all the Hubs is the prerogative of acceleration in material development,[15,47] and therefore, by following this design philosophy, our Auto-MISCHBARES platform is able to perform fully autonomous electrochemical measurements tailored to study the formation of CEI and

monitor oxidation state changes in active materials at different stages of the experiment.

4.1.1 DeviceHub. In this study, the core of our DeviceHub is an electrochemical system known as SDC.[42] This setup is an open-cell miniaturized 3-electrode-cell construction comprising a gold reference electrode (RE) and a platinum counter electrode (CE), both positioned within a movable cell housing made from polytetrafluoroethylene (PTFE). This housing utilizes electrode spots on a planar substrate functioning as the working electrode (WE). The SDC is connected to a stepper motor ‡ and a multichannel potentiostat device §. Additionally, the DeviceHub encompasses a syringe pump system ¶, which is connected to this cell *via* an inlet. Our configuration allows for precise delivery of the desired electrolyte formulation, as well as enabling accurate positioning over the targeted measurement area on the WE substrate and the deposition of a single droplet of electrolyte. Upon contact of all three electrodes, the system is ready to execute the selected protocols (Fig. 1b, section setup). The placement of the SDC and measurement through the potentiostat are controlled by the ServerHub.

4.1.2 ServerHub. This platform is an advanced extension of our initial ServerHub presented in HELAO.[30] It is capable of executing experiments both sequentially and in parallel, and allows for the integration of an active learning decision-maker to orchestrate tasks across instruments. The complete workflow is illustrated in Fig. 1a. At the beginning, researchers configure experimental setups and schedule multiple, dynamic batches of experiments through a user-friendly and modular interface (ESI 1†). The UI is constructed using HTML, and CSS with dynamic functionalities implemented in Node.js and facilitates easy browsing with a diverse array of electrochemical protocols. This interaction layer is further enhanced by Flask,[48] a Python-based web framework, to streamline user engagement. Once single or multiple experimental batches are designed, the configurations are passed to the Python back-end, requiring no additional user intervention, and are translated to FastAPI requests. The central orchestrator will then efficiently schedule and manage high-throughput experimentation in an asynchronous manner. After the execution of all requested experimental batches, the operator receives a response from the orchestrator with a comprehensive report detailing all experimental steps, their timestamps, and outcomes.

4.1.3 MultiAnalyticHub. A key challenge in automation is maintaining the reliability of results, which is crucial for managing potential risks since a plethora of variables and parameters are prone to errors during experimentation.[2] These include tasks typically simple for humans, such as removing salt accumulation, replenishing depleted electrolyte bottles, ensuring electrical connection at the hardware level, and maintaining safe thresholds for measurement parameters at the software level. Failure to address these aspects could lead to experimental inaccuracies and substantial time and resource wastage. Mitigation strategies are a crucial aspect in the realization of a truly autonomous laboratory.[47] Thus, our MultiAnalyticHub is equipped to enhance the platform by implementing mechanisms for providing critical feedback through automated quality control (QC) and real-time analysis throughout the experimental stages (Fig. 1b, Section Quality Control & Analysis). This Hub aims to inform researchers of ongoing progress and potential failures and provide accurate, statistically driven analysis, increasing trustworthiness in high-throughput experimentation.

The initial QC assessment in our system is monitoring material sufficiency at the electrolyte exchange stage for each measurement. A key component of this process is the Droplet Detection routine, designed to verify proper flushing. This detection is implemented using the OpenCV library[49] for computer vision tasks and analyzes a video streams to detect the presence of a drop.[50] The algorithm selects a specific region of interest (ROI) in the video frame, converts this segment into grayscale, and applies a Gaussian blur to minimize noise. By continuously calculating the absolute difference between the initial frame and subsequent frames within the ROI, the system can detect motion. A non-zero sum in the thresholded image within this area indicates of a drop's presence. The selection of a ROI is motivated by two main reasons. The reduction of computation time by focusing on a small area of the output and the elimination of false positives that may arise due to motion detection in the background of the camera. Given that the SDC movement is motorized, and the material is flushed at a predefined position, the ROI is calibrated only during the setup phase and remains unchanged throughout the experimentation. In addition, visual feedback is provided on the monitor for user verification and oversight.

Once the electrolyte has been exchanged, a non-negligible chance persists of residual material remaining attached to the head of the SDC, which can lead to salt formation, crystallization, or inconsistencies in later measurements. We expanded our quality control protocol and incorporated a mandatory movement of the SDC head to a wiping pad, ensuring the removal of any leftover electrolytes. Following this preparation, the stepper motor positions the SDC head over the designated measurement area of the WE (Fig. 1b, section automated experiment).

Additional QC is implemented to control the movement of the SDC head precisely and ensure optimal electrical connectivity with the substrate in the coming measurement. This mechanism is designed to lower the SDC head gradually, performing the descent in small, constant steps. This approach secures each movement to stay within a defined threshold to prevent excessive force on the head. For stepwise monitoring of electrical potential, frequent control measurements are integrated with potentiostatic endpoints of the ServerHub. The voltage data is then used to determine successful contact with the substrate, indicated by a sharp decay in potential towards zero. If contact is not established within the initial steps, the routine initiates corrective measures. These include the controlled addition of electrolytes, periodic potential

‡ https://www.owis.eu/en/.

§ https://www.metrohm.com/de_de/products/a/ut30/aut302n_s.html.

¶ https://www.hamiltoncompany.com/laboratory-products/microlab-600/syringe-pump.

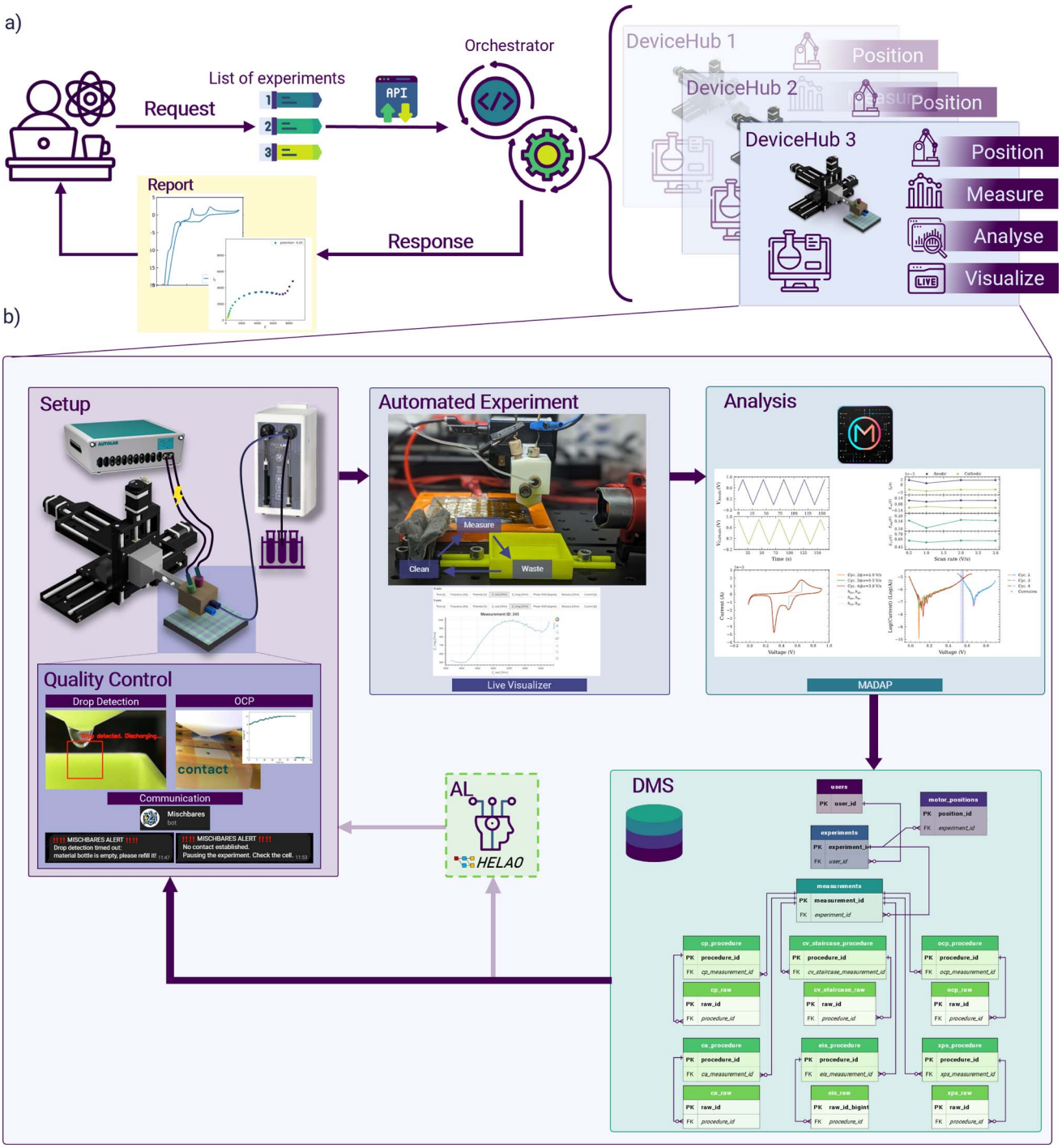

Fig. 1 Schematic representation of the experimental setup and automated flow of Auto-MISCHBARES.[44] The interface (ESI 1†) allows researchers to formulate a series of experimental electrochemical protocols, which are then dispatched to a central orchestrator *via* an API. The orchestrator, serving as a control system, manages the scheduling, execution, and monitoring of the experimental array by delivering actions to the individual Hubs, which are the granular unit of activity and can execute actions tasks such as positioning, measurement, real-time analytical processing and provides the basis for live visualization. Upon the completion of individual experiments or a sequence thereof, the orchestrator compiles and dispatches a comprehensive analytical report to the experimentalist. The DeviceHub features a high-precision robotic manipulator adept at positioning the SDC head accurately onto the substrate, where a Hamilton Microlab 600 precision syringe system[3] delivers electrolyte directly when contact is established. The Autolab Potentiostat[2] is employed to perform electrochemical measurements once the system is primed for analysis. Quality control protocols, including drop and contact detection and chatbot-based communication, facilitate automation and oversight of the experimental processes. Furthermore, experiments proceed in three automated stages: waste disposal, cleaning, and electrochemical measurement, each executed according to predefined specifications and with real-time plotting provided by a Bokeh[45] visualizer for immediate "at-a-glance" feedback. Post-measurement, the data undergoes immediate analysis *via* MADAP, which calculates electrochemical markers and generates corresponding plots for in-depth analysis. This processed data is then systematically cataloged in a DMS, ensuring data provenance, facile retrieval, and compartmentalization in alignment with the FAIR principles. It is possible to optimize the subsequent experiment with AL algorithms through the HELAO platform.

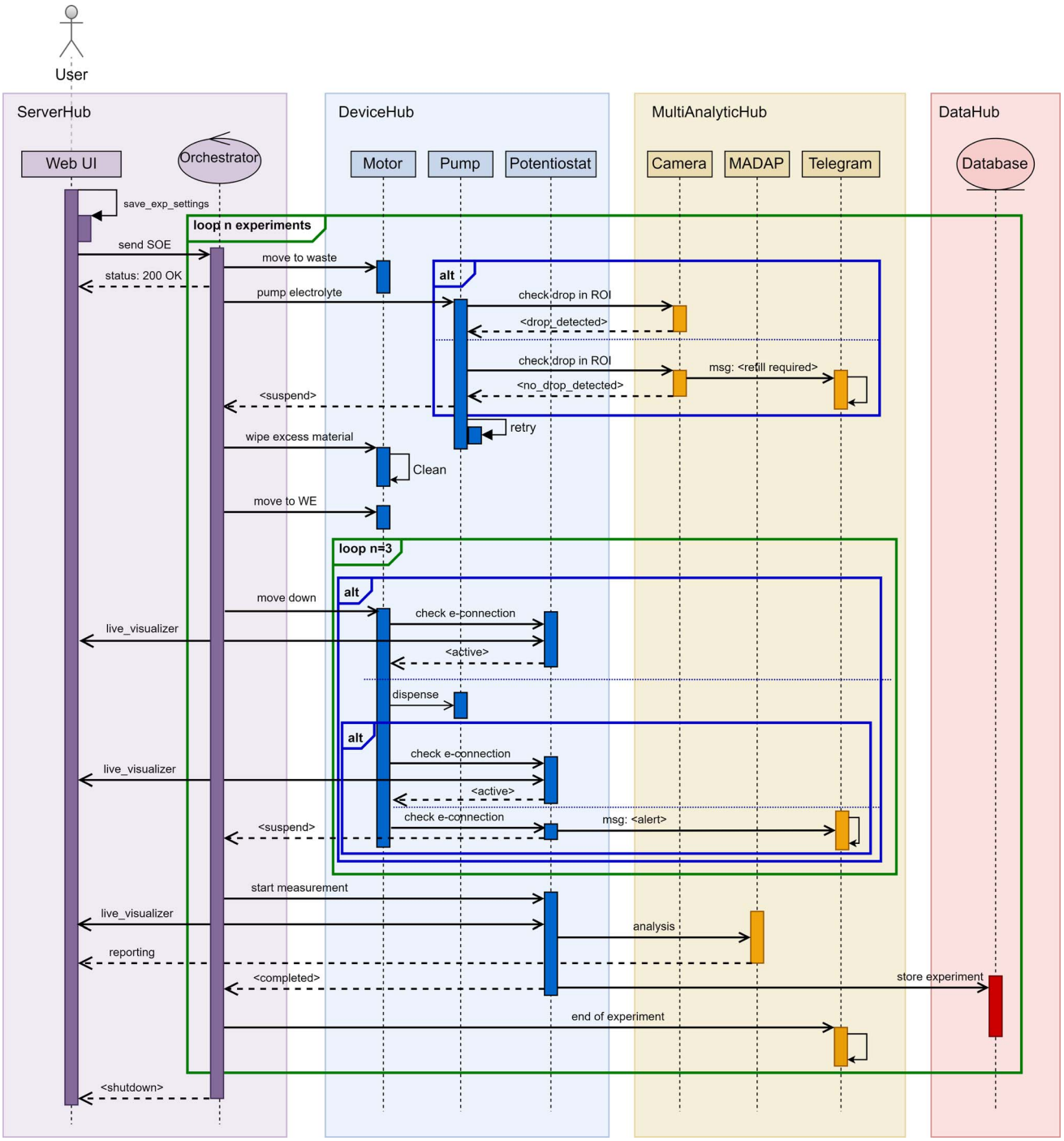

Fig. 2 A sequence diagram representing the interaction between the different proposed Hubs in the Auto-MISCHBARES framework for the showcased automated experimentation. The web-UI and the orchestrator represent lifelines and are active throughout the experimentation process. After the user has made the experimental configuration, the settings are saved, and the interface sends the SOE asynchronously to the orchestrator, which initiates the movement by sending the instruction to the motor in the DeviceHub. The motor moves to a predefined waste position, where a pump dispenses electrolytes for the desired experiment. Asynchronously, the presence of material will be checked in the ROI of the camera where the algorithm is executed on its lifeline in the MultiAnalyticHub. Depending on the outcome, the experiment might be suspended, and the user notified about the absence of material over a Telegram chatbot. After a predefined waiting time, the pumping is retried. Once drop detection is successful, orchestration resumes with a mandatory movement to the wiping pad to remove excess material and subsequent positioning on the WE. Here, an additional quality control loop is implemented, joining the DeviceHub to the MultiAnalyticHub in the case of absent electrical contact. Herein, the connection is checked while the SDC head is moved downwards. If successful, the experiment can proceed. Mitigation strategies in case of non-contact are planned to dispense small amounts of electrolyte and additional connection checks. All the attempts are displayed in a live visualizer activated in the ServerHub. Ultimately, if no connection is established, the experiment is suspended, and the user is notified. A successful contact is a prerogative to start the measurement, which is asynchronously analyzed by MADAP in the MultiAnalyticHub, reported to the ServerHub for visualization, and stored in the DataHub. The live visualization continues throughout the

measurements, and emergency procedures in place for unresolved non-contact situations. Upon measurement initiation, an established safety threshold for experimental procedures prevents overshooting. Throughout the entire QC process, continuous feedback is provided with logging and the option of communication through a Telegram chatbot, which update the experimentalist at checkpoints and about potential failures, especially beneficial of walk-away experimentation.

Our previously designed modular and versatile data analysis framework, MADAP,[51] capable of analyzing a variety of electrochemical protocols, is additionally integrated into the MultiAnalyticHub of our high-throughput automated workflow. It enables the real-time transformation of raw measurement into analyzed results for each experiment. The strength of this framework lies in its ability to simultaneously plot the raw and processed data (Fig. 1b, section analysis). The integration of this modular package was a facile solution for Auto-MISCHBARES to gain the ability to generate reports and summaries in compliance with FAIR principles, expanding the platform to include rapid assessment of experimental quality for valuable scientific insights.[3,46] Tailored to our case study, MADAP was expanded with voltammetry tests that include the statistically driven identification of parameters as, for instance, half-wave potential and current, peak-to-peak separation, oxidation and reduction peaks to include them in the report. Additional information about the expanded implementation can be found in ESI 5.†

4.1.4 DataHub. The provenance of data is central in drawing conclusions from raw experimental recordings.[29,52,53] This necessitates active tracking of acquisition and processing. To address the challenge of managing these complexities, our DMS implements a real-time approach in the context of the DataHub, which is backed by a locally hosted PostgreSQL database designed to dynamically handle meta, raw, and analyzed data. It consists of several interconnected tables that capture specific details of the proposed experiments. The *experiments* table forms the core of the database and stores essential metadata, such as material, date, and operator information (Fig. 1b, Section DMS). This is complemented by the *users* table, which details the researchers involved, ensuring traceability and accountability. The *motor-positions* table logs the specific operational data, such as precise motor positions of the SDC head, adding further detail to the experimental records. Each type of electrochemical measurement in the database features paired procedures and raw tables. The *procedure* tables encapsulate the unique parameters and settings of every measurement, while the *raw* tables record granular empirical data. Key metrics, provided by MADAP from the MultiAnalyticHub and passed to HELAO in the ServerHub, support processing large data volumes through web server communication. Robust data integrity is ensured through primary and foreign keys, enabling complex queries that link procedures, raw data, and experimental metadata. Additionally, the database incorporates sequences for auto-generating Unique Identifiers (UIDs), streamlining data entry and retrieval. This cohesive database system is designed to maintain the integrity, accessibility, usability, and interpretability[54] of experimental data by incorporating both FAIR principles[36] and atomicity, consistency, isolation, and durability (ACID) standards[55] for modern data management and reliable operational processing. Herein, the DataHub offers a unified platform for comprehensive multi-modal data analysis engineered to facilitate the correlation of electrochemical and spectroscopic tests.

The integration of the four key Hubs defines our robust Auto-MISCHBARES platform,[44,50] streamlining sequential experimentation through unified process control, scheduling, feedback, and advanced real-time data management, encompassing measurement, validation, and analysis. Herein, experiments are started in the ServerHub, which schedules and orchestrates the measuring step performed by the instruments in the DeviceHub. The procedure is controlled for its quality and analyzed for its outcome by the MultiAnalyticHub while the DataHub records all trackable data points. A detailed representation of the asynchronous interaction between these Hubs is depicted as a sequence diagram in Fig. 2. The modular design of Auto-MISCHBARES as an open-source Python framework and multiple unit-tests ensure ease of expansion and adaptability for users.

4.2 Experimental procedure

To showcase the efficacy of Auto-MISCHBARES, we investigate the formation of the CEI, as it is influenced significantly by the type of active material, the inactive components of the composite electrode, and the electrolyte formulation.[56,57] The presented electrochemical setup, SDC, eliminates the need for cell disassembly for *ex situ* measurements, thus minimizing the risk of mechanical alterations. To demonstrate the reliability and reproducibility of our proposed Auto-MISCHBARES framework, we investigate the evolution of CEI in lithium iron phosphate (LFP), a well-studied cathode material used in commercial batteries.[58–60] We used 1 M $LiPF_6$ solution in a mixture of ethylene carbonate (EC) : ethyl methyl carbonate (EMC) in a 3 : 7 weight ratio as the electrolyte (E-lyte, Germany). The entire setup was maintained in a nitrogen-filled glovebox. It is important to note that electrolyte evaporation can occur due to the open-cell setup. This poses challenges for long-term cycling tests, however, it offers distinct advantages for a variety of short-term measurements, which would otherwise require extensive assembly, disassembly, and electrode post-treatment. We designed our high-throughput sequential experimentation protocol using cyclic voltammetry (CV) tests, which are stopped at different potentials during the second cycle to analyze features related to redox reactions and repeated the procedure two times. Our novel approach to cathode electrode preparation involves screen-printing onto the substrate in

measurement. Orchestration now considers the experiment complete, will notify the user, and will move to the next instance defined in the SOE. The process is repeated until the experimental list defined by the research is completed. The orchestrator will shut down all remaining active components, and details of inputs, outputs, and metadata will be saved in .hdf5 formatted file.

an open atmosphere due to the stability of the active material and slurry components. This method minimizes material usage and precisely defines the active material area. After preparation, the electrodes are transferred to the glovebox for further processing and analysis. For each experiment, the SDC head is positioned at the predefined measurement spot, where it dispenses a droplet of electrolyte and ensures electrical connection before performing CV. Upon completing a series of experiments, it is necessary to remove the excess $LiPF_6$ salt residue, a byproduct of electrolyte evaporation, from the electrodes. This is achieved by depositing a droplet of propylene carbonate (PC) on each measurement spot, allowing it to soak for three minutes to dissolve the salt, and then aspirating it using the SDC head. This cleaning process is repeated three times. Once the cleaned samples are dried, they are transferred within the glovebox directly into the XPS's sample environment for *ex situ* analysis, preventing air exposure. The analysis aims to characterize the synthesized CEI at different potentials and identify the formation stages of its components. The CasaXPS software[61] is utilized to evaluate the outcomes.

5 Results and discussions

5.1 Reproducibility towards electrode fabrication

In our setup, electrodes were fabricated through screen-printing to ensure reproducible dimensions and alignment on a predefined grid. This method effectively decouples the electrodes from the electrolyte spreading area, thereby minimizing cross-contamination risks associated with electrolyte dispersion on the substrate. Additionally, this technique significantly reduces waste of active material. Unlike other coating methods such as doctor blading, which produce cut-out waste, screen-printing only coats the specific spots required for measurements.

The electrodes were coated as circular points with a 1.5 mm diameter, arranged in an 11 × 11 square grid with each point spaced 4.9 mm apart. Details can be found in Section 4 of the ESI.† To evaluate the uniformity of the coating, these electrodes were analyzed using XRF. Fig. 3a illustrates the distribution of Fe signal intensity across the grid, with the colorbar reflecting the relative Fe content as determined by the integrated signal at each point. As a direct measurement of the active material mass on this type of coating is challenging, the Fe signal in XRF images was used as a proxy for estimating Fe distribution and the active material content. By weighing the Al-foil before and after coating and drying, an average active material mass of 0.0218 mg was calculated. The Fe count per second (CPS) is centered around a central peak, indicating an underlying normal distribution with a maximum spread of ±6.5%, as depicted in Fig. 3c. Our two distinct sets of measurements are represented by red and blue markers in Fig. 3a. The color distribution across the grid indicates a uniform Fe coating, although some areas exhibit higher or lower concentrations. This is crucial for evaluating the consistency of the screen-printing process. The XRF spectrum of a representative coated point is shown in Fig. 3b and features Fe peaks at 6.41 keV and 7.06 keV. While the spectrum is primarily characterized by Fe, minor peaks for Cr and Ni indicate their subordinate presence. Additional elements including P and Al, with peaks at 2.02 keV and 20.19 keV respectively, are also identified. The peaks, with lower CPS, are detailed in ESI 3.† In the electrochemical

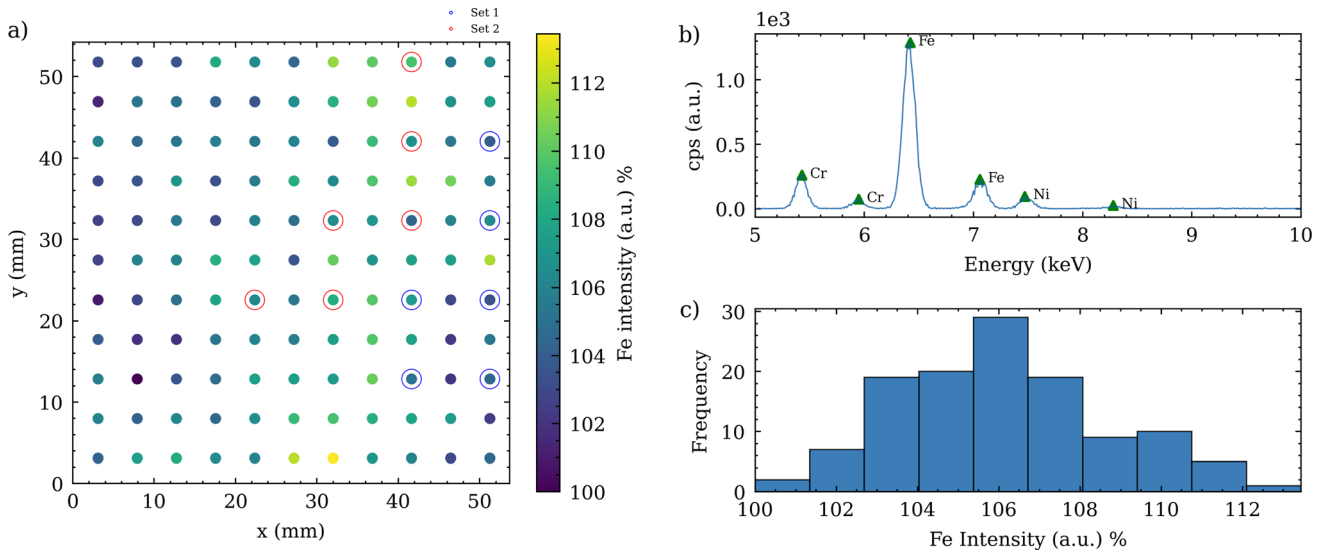

Fig. 3 (a) Spatial distribution of the integrated relative Fe signal intensity from screen printed electrodes, as measured by XRF. The Fe signal is integrated over a circular area of 1.8 mm in diameter at each measurement point, with color coding indicating the intensity percentage. Set 1 and Set 2 refer to two different batches under which the electrodes were tested, showcasing potential variability in Fe distribution across the samples. (b) Averaged XRF spectrum representing cumulative signals from one of the screen-printed spots, highlighting characteristic X-ray peaks. Peaks are labeled with corresponding elemental symbols, with prominent feature for Fe observed at around 6.4 keV. Other elements such as Cr and Ni are represented at their respective energies, illustrating the composition of the samples. (c) Histogram representing the distribution of Fe intensity percentages across the measurement points. The distribution shows a rightward skew, with a predominant concentration of data points on the lower side of the Fe intensity scale. Despite the skew, the bulk of the data clusters around a central peak, suggesting an underlying normal distribution tendency with some deviations, possible due to variations in the screen-printing process or material heterogeneity.

procedures, such as galvanostatic cycling, this data can be utilized for setting the correct current to achieve the desired C-rate during charging and discharging protocols. For CV, as employed in this study, the information is essential to normalize the obtained current response.

5.2 Reproducibility at electrochemical level

Electrochemical data that derived from the automated experiments orchestrated with Auto-MISCHBARES platform demonstrated high reliability, with no observable failures or hardware errors that could compromise the results. All the measurements are stored on-the-fly in our DMS. The CV profiles of LFP electrodes, cycled between 1.8 V and 4.7 V at a scan rate of 5 mV s^{-1} are presented for two identical experimental sets for comparison, as shown in Fig. 4a and b. The scan rate selected for our study was an order of magnitude higher than typically reported for battery electrodes.[62] This choice aimed to mitigate issues associated with electrolyte evaporation in our open setup. Such evaporation could disrupt electrical contact between the WE and the RE during measurement and increase salt concentrations in electrolyte.[63] However, these effects were minimized by using a fast scan rate and routine flushing of the SDC head with fresh electrolyte after each measurement. The high scan rate can cause the change of slope in current density for CV measurements.[64]

In both sets of experiments, anodic and cathodic peaks were observed at approximately 3.8 V and 3.15 V, respectively, with a characteristic pair of redox peaks around 3.47 V corresponding to the charge–discharge reaction of Fe^{2+}/Fe^{3+}. In the first set, a minor anodic peak at 4.4 V was also detected, the origin of which remains unclear but aligns with findings reported by Chen *et al.*[65] Our observed peak values, including anodic ones at 3.7 V, cathodic ones at 3.25 V, and half-wave potentials of 3.4 V at a scan rate of 0.1 mV s^{-1}, closely match those documented in their study. It is also important to mention that the reference potential was calibrated against a 5 mM ferrocene solution prior to experimentation.

In the first set of experiments, a slight shift in anodic peaks was observed, while the cathodic peak potential remained constant. The slight increased peak to peak separation, suggests lower reversibility,[66,67] likely due to the higher scan rate[62,64] used in our measurements. However, the experiments were able to replicate features documented in related literature.[65,66] The growing asymmetry in peaks, observed as measurements progressed, can be attributed to increasing conductivity constrains,[65] a result of SEI growth at the CE and the RE, as these were not exchanged between measurements. In the second set of experiments, consistency was observed across all CV tests, with only minor variations in samples 4 and 5. The half-wave potential and peak separation showed a slight shift towards higher values. These changes in polarization might be partially attributed to the distance between the WE and the RE,[68] or to an uneven substrate. Despite these complexities, the overall results from the SDC demonstrated a high degree of reproducibility across both sets of experiments. The synthesized CEI outcomes from these data are suitable for further exploration using *ex situ* techniques.

5.3 Reproducibility at spectroscopic levels

Upon completing both sets of electrochemical experiments, the electrodes were rinsed with a PC solution, using SDC system to remove any residual dried electrolyte. After drying, an *ex situ*

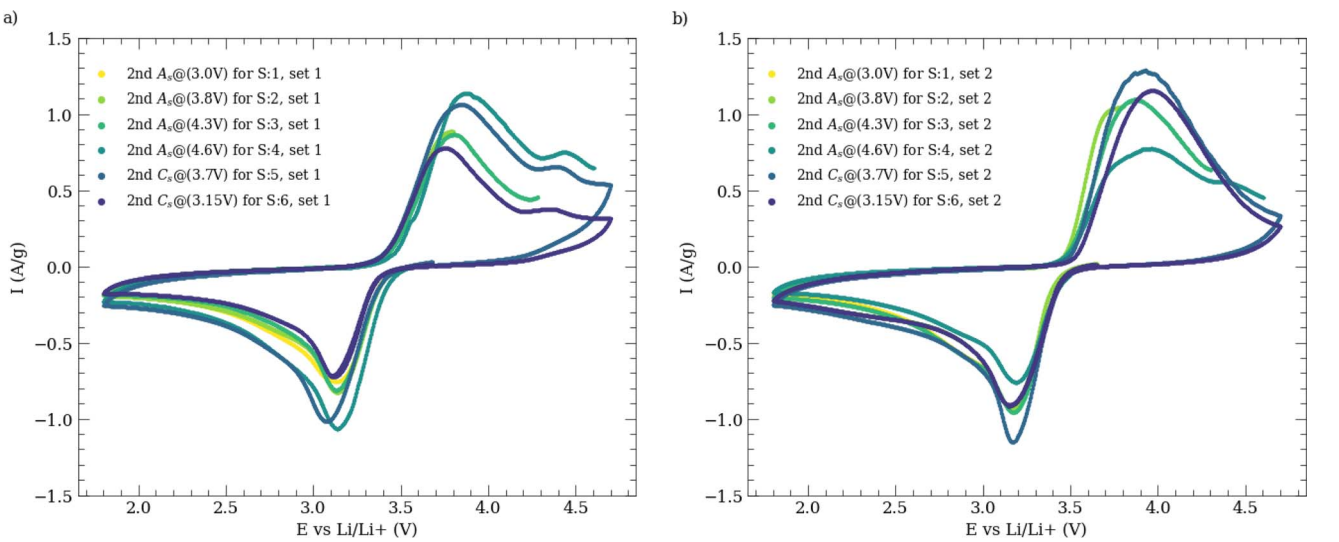

Fig. 4 Demonstration of the second cycle of CV profiles derived from high-throughput experimentation utilizing Auto-MISCHBARES. Experiments were applied within a voltage range between 1.8 V and 4.7 V at a scan rate of 5 mV s^{-1}, starting from the OPC in the anodic direction. The CV curves reveal distinct redox peaks and the anodic peaks align closely at approximately 3.8 V while the corresponding cathodic peaks are positioned near 3.15 V, indicating similar consistent electrochemical response with a high degree of overlap across all measurements. (a) illustrates the first set and (b) the second, with each set consisting of six different experiments. For comparative analysis, CV tests that conclude at the same stop potential between the two batches, are color-matched. The exact termination potentials, corresponding to either the anodic or cathodic directions, are denoted in the legend. The reported current density is normalized to the mass of LFP, determined by XRF measurements of the Fe signal as a proxy for the LFP content.

XPS analysis was performed on the initial experimental set to evaluate the development of the CEI. This analysis identified various species and functional groups, as demonstrated in Fig. 5a across all panels, which presents the spectra from sample 1 (S1) of this set. The C═C peak, representative of the conductive carbon at the electrode surface, was selected as the reference with a relative concentration of 1. All subsequent signals are scaled and normalized to this benchmark.

Within the C 1s region (Fig. 5a, panel I), a variety of carbon-containing species were identified. Peaks at 284.3 eV and 284.8 eV correspond to sp^2 (C═C) and sp^3 (C–C) carbon bounds, respectively. Additional peaks at higher binding energy, such as 286.3 eV, 288.8 eV, and 290.7 eV, were assigned to C–O, carboxyl (O–C═O), and carbonates CO_3 groups. In other samples of this set, a C═O signal was also detected near 287.8 eV (ESI 7 and 9†). These signals are complemented by corresponding peaks in the

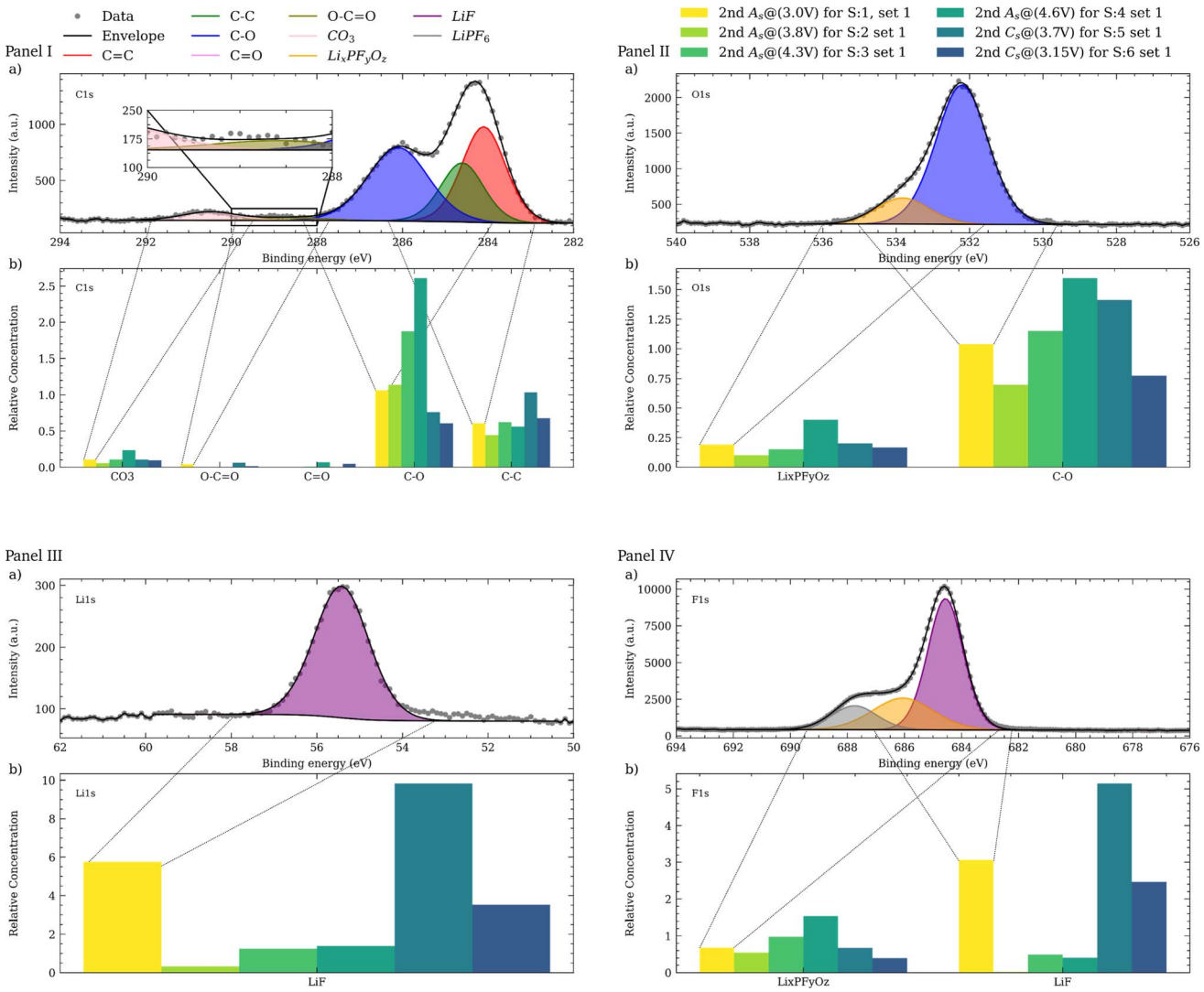

Fig. 5 Characterization of the synthesized CEI from Auto-MISCHBARES on screen-printed electrode using *ex situ* XPS analysis. In all panels, (a) present the XPS spectra of CEI from sample 1 (S1) in the first experimental series, obtained during the second anodic scan at the stopping potential of 3 V from the CV test. These spectra reveal the diverse chemical composition of this layer, with peaks corresponding to various functional groups and compounds: (panel I) C 1s spectrum with multiple peaks indicative of carbon-based species, including C–C, C–O, and contributions from other carbon-oxygen groups. (Panel II) The O 1s spectrum with a peak for C–O bonds. (Panel III) The Li 1s region with presence of lithium-containing compounds depicted by LiF peak, originating from the decomposition of $LiPF_6$. (Panel IV) The F 1s region characterized by peaks associated with fluorinated compounds. Each chemical state identified is denoted by a distinct color in the spectra. The overlaid black line represents the envelope of the aggregated measured data, indicating the sum of contributions from all fitted peaks. The bottom bar charts (b) provide a comparative analysis of the evolution of XPS signals for various species, observed from the first set and aligned by sequence of appearance in the CV tests, illustrating the binding energy signatures of specific chemical states within the CEI with relative concentration at these regions. The C═C peak intensity is set as a reference with the relative concentration of 1, representing the conductive carbon additive at the electrode surface, with other species normalized to this reference. The relative concentration of C–O in the C 1s region shows a significant increase from sample 2 (S2) to sample 4 (S4), followed by a decrease in sample 5 (S5). In contrast, the LiF signal in the Li 1s and F 1s regions decreases up until S4 and then exhibits a sharp increase from S4 to S5. The behavior for $Li_xPF_yO_z$ species in the O 1s and F 1s regions follows a similar pattern to that of the C–O group.

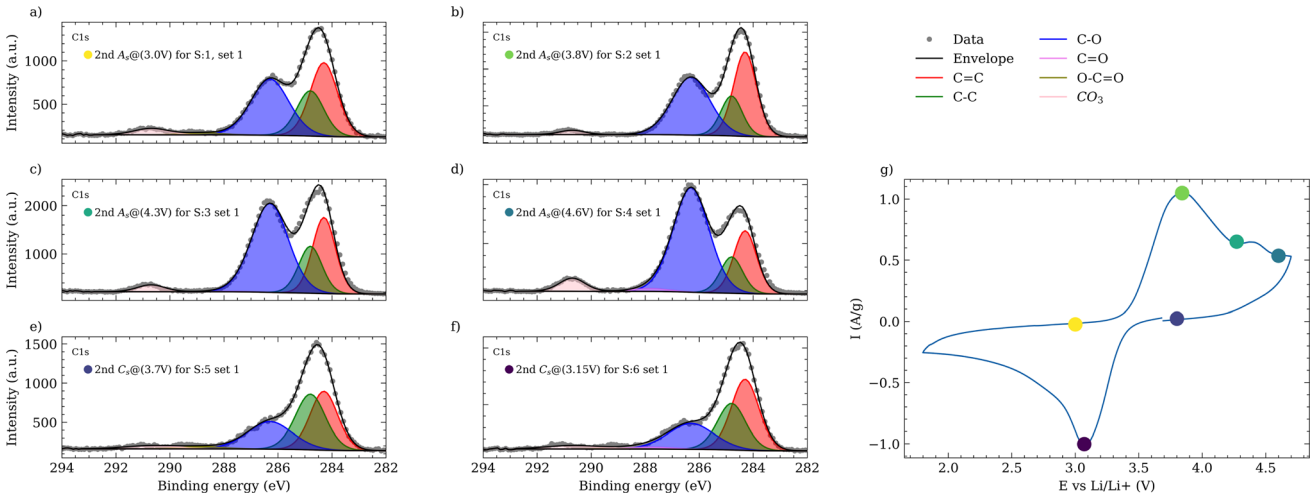

Fig. 6 Representation of the XPS spectra in the C 1s region for all samples from the first set of high-throughput experimentation (a–f). The key potentials at which measurements were paused during the second cycle of CV test are depicted in (g). During the anodic scan (a–d), an increase in the intensity of signals from organic species, such as C–O, is observed, indicative of the evolving composition of the CEI. During the cathodic scan (e and f), this intensity decreases significantly.

O 1s region, with a major contribution from C–O bonds, centered at 532.4 eV (Fig. 5a, panel II). In the F 1s spectrum (Fig. 5a, panel IV), the residuals from the $LiPF_6$ salt is discernible at 688.0 eV. The remaining salt from the rinsing process suggests a need for further investigation by utilizing EMC or dimethyl carbonate (DMC) to potentially enhance the efficiency of the washing procedure, due to their higher $LiPF_6$ and lower LiF solubility. In the O 1s region, fluorophosphates, as degradation products of $LiPF_6$ observed at 534.0 eV, with corresponding signals at 686.6 eV in the F 1s region. The signal for LiF, indicating the presence of fluorinated and lithiated species, is evident at 684.8 eV in the F 1s and 55.6 eV in the Li 1s region (Fig. 5a, panel III). The similarity between the C–O and $Li_xPF_yO_z$ compounds reflects the dynamic alterations of the CEI composition throughout the electrochemical cycling process.

Fig. 5b for all panels, illustrate the evolution of the XPS signals across all the samples of this series. During the anodic scan of the CV measurement, an increase in the intensity of signals from organic species, such as C–O is observed in both C 1s and O 1s regions. These signals are attributed to the decomposition products of the electrolyte and contribute to the formation of the outer layer of the CEI. Notably, the increase in these signals becomes apparent in S3, at 4.3 V, coinciding with the peak of the anodic feature and subsequent potential elevation, consistent with findings reported by Kühn *et al.*[56] In contrast, during the cathodic scan, the intensity of these species decreases significantly from 4.6 V to 3.7 V. This pattern further supported by Fig. 6, exhibiting the C 1s trends across all samples. The observed increase in organic species during the anodic scan is indicative of a thickening of the CEI, presumably due to electrolyte decomposition at elevated voltages, which is supported by several studies[69–72] and evidenced by the reduced LiF signal from S1 to S4 (Fig. 5b, panel IV). During discharge, the cathodic scan shows an increasing LiF signal, suggesting the reformation of LiF, along with a decrease in C–O species.[73]

At last, the XPS analysis validates the electrochemical data at every potential, pinpointing key regions within the CV profile. This correlation further enhances the integrity of our designed Auto-MISCHBARES workflow, contributing to the robustness and advancement of MAPs.

6 Conclusions

A critical question that arises with high-throughput platforms is whether they truly accelerate processes or inadvertently cause deceleration. Answering this, requires considering three key aspects: reliability, time efficiency, and reproducibility. Regarding reliability, Auto-MISCHBARES, represents a significant advancement in laboratory automation and scientific experimentation by integrating a comprehensive array of key components for robust, sequential experimentation. It covers a wide range of functionalities, from configuring and scheduling experiments to robust online control assessment, and provides real-time feedback on critical failures and experimental progress. Encompassing computer vision and statistical tools, the platform not only ensures the reliability of outcomes but also streamlines tasks to minimize researcher intervention and reduce human errors. Its real-time measurement capabilities, enable live visualization and can further optimize the workflow, from data acquisition to comprehensive analysis. The structured PostgreSQL database environment within the platform efficiently manages data formats, strengthen data correlation across multiple measurements and lays the ground for transfer learning. In our SDC system, the modifications to mechanical integrity are minimal as opposed to coin cell setups where disassembly can lead to the breaking of coatings at the edges of the electrodes, and sometimes even cause the coating to stick to the separator. Our SDC system is a more reliable and less intrusive approach to cell handling and is suitable for applications in electrochemical studies.

To establish time efficiency, our hierarchical framework demonstrates significant advantages due to its uninterrupted operational capabilities, which minimize the need for manual cell exchanges. For instance, considering our study scenario where our substrate consists of 121 electrode spots, each requiring a one-hour CV test. In this case, our Auto-MISCHBARES platform, using the SDC head, would complete the measurements in 121 hours, with an additional 10 hours for rinsing, and moving for a total of 131 hours. In contrast, the traditional manual approach would require extra time for cell assembly and disassembly, which takes an experienced researcher an additional 24 hours. Assuming an 8 hour workday without breaks, the manual process would span several days. Additionally, considering the limitation of processing only about 10 coin cells simultaneously due to channel availability in the cycler, this manual approach could extend the duration even further. While the measurement times are similar between our platform and manual methods, our framework's ability to operate continuously substantially enhances the time efficiency. As demonstrated in our previous study,[30] the capability of our framework for parallelization across multiple SDCs as well as its integration with AL frameworks can further accelerate the process.

To address the final aspect of reproducibility, our platform proves validity in both electrode fabrication and electrochemical measurements. The use of screen-printing to create miniaturized, defined areas of measurement not only saves materials but also facilitates automated *ex situ* analysis. This is attributed to the precisely arranged grid of measurement positions established by the screen-printed mask on the substrate. Further enhancements in future studies can be achieved by integrating XRF measurement results into the platform, allowing for the identification of mask defects and the selection of points with minimal deviation, thus reducing issues related to electrode thickness variation. Such variations can also affect the distance between the WE and RE, potentially leading to deviations in measurements.[64] These challenges can be further minimized by directly coating onto the substrate holder and avoid the use of a bendable foil for electrode fabrication. The consistency of our high-throughput electrochemical protocols, along with their correlation with XPS results that align with findings in the literature, further underscore the reproducibility and fidelity of our system. Auto-MISCHBARES enables in-depth investigation into the synthesis of SEI/CEI, especially for post-lithium battery materials, an area that still holds vast potential for exploration. It should be noted that the proposed electrochemical experimentation setup is bound by the availability of the measurement devices and their licensed software. However, through the modularity and agnosticism of the platform, Auto-MISCHBARES can be expanded with minimal effort following the provided templates to include any laboratory device needed for any specific experimental scenario.

Integrating the comprehensive capabilities of our platform, we establish a trustworthy foundation with online analytical characterization, robust data fidelity and management systems. This integration facilitates the incorporation of ML and AL algorithms, enhancing decision-making and accelerating material optimization. Our hierarchical web server framework, which has been previously integrated with AL, now allows for further integration with more complex experimental planning algorithms such as Chimera[74] and Griffyn.[75] Additionally, for future study, the inclusion of cutting-edge approaches such as large language modeling (LLM) can further assist researchers,[13] steering us towards the ultimate goal of a fully reliable material acceleration platforms. Our user-friendly framework, committed to digitalization and technological integration, represents a crucial step towards the development of fully autonomous laboratories, which can significantly expanding the scope of scientific exploration.

Additional information

Additional information can be found in the ESI.†

Data and code availability

Data, supporting the findings of this study, are available online at **https://doi.org/10.5281/zenodo.10444324**. The Auto-MISCHBARES framework[44] can be cloned from **https://github.com/fuzhanrahmanian/MISCHBARES**. In addition, videos recorded from our fully autonomous workflow[50] can be accessed at **https://doi.org/10.5281/zenodo.10445749**.

Author contributions

F. R. conceived the experiments, design the data analysis MADAP and Auto-MISCHBARES software, developed the quality control protocols, validation tests, and user interface. H. S. S. prepared the mask for screen printing. B. Z. designed and printed the waste, wipe, and camera housing. S. F. prepared the electrode material and coated them onto the printed mask. F. R. and S. F. assisted in experimentation and S. F. characterized the samples by applying XPS. All authors reviewed the manuscript.

Conflicts of interest

The authors declare no conflict of interest.

Acknowledgements

This work contributes to TUM Battery, the Munich Data Science Institute, and the Munich Institute for Robotic and Machine Intelligence. This work contributes to the research performed at CELEST (Center for Electrochemical Energy Storage Ulm-Karlsruhe) and was partly funded by the German Research Foundation (DFG) under Project ID 390874152 (POLiS Cluster of Excellence). This project also received funding from the European Union's Horizon 2020 research and innovation program under grant agreement No. 957189. The project is part of BATTERY 2030+, the large-scale European research initiative for inventing sustainable batteries for the future, funded by European Union's Horizon 2020 research and innovation program under Grant Agreement No. 957213 (BIG-MAP). HSS

acknowledges funding from German Research Foundation (DFG) under Project ID 390776260 (eConversion Cluster of Excellence).

Notes and references

1 H. S. Stein, *Trends Chem.*, 2022, **4**, 682–684.
2 E. Stach, B. DeCost, A. G. Kusne, J. Hattrick-Simpers, K. A. Brown, K. G. Reyes, J. Schrier, S. Billinge, T. Buonassisi, I. Foster, *et al.*, *Matter*, 2021, **4**, 2702–2726.
3 L. M. Roch, F. Häse, C. Kreisbeck, T. Tamayo-Mendoza, L. P. Yunker, J. E. Hein and A. Aspuru-Guzik, *PLoS One*, 2020, **15**, e0229862.
4 M. Seifrid, R. Pollice, A. Aguilar-Granda, Z. Morgan Chan, K. Hotta, C. T. Ser, J. Vestfrid, T. C. Wu and A. Aspuru-Guzik, *Acc. Chem. Res.*, 2022, **55**, 2454–2466.
5 A. E. Gongora, B. Xu, W. Perry, C. Okoye, P. Riley, K. G. Reyes, E. F. Morgan and K. A. Brown, *Sci. Adv.*, 2020, **6**, eaaz1708.
6 P. Nikolaev, D. Hooper, F. Webber, R. Rao, K. Decker, M. Krein, J. Poleski, R. Barto and B. Maruyama, *npj Comput. Mater.*, 2016, **2**, 1–6.
7 A. Dave, J. Mitchell, S. Burke, H. Lin, J. Whitacre and V. Viswanathan, *Nat. Commun.*, 2022, **13**, 5454.
8 Y. Shi, P. L. Prieto, T. Zepel, S. Grunert and J. E. Hein, *Acc. Chem. Res.*, 2021, **54**, 546–555.
9 M. Abolhasani and E. Kumacheva, *Nat. Synth.*, 2023, **2**, 483–492.
10 S. Ament, M. Amsler, D. R. Sutherland, M.-C. Chang, D. Guevarra, A. B. Connolly, J. M. Gregoire, M. O. Thompson, C. P. Gomes and R. B. van Dover, *Sci. Adv.*, 2021, **7**, eabg4930.
11 R. Ramprasad, R. Batra, G. Pilania, A. Mannodi-Kanakkithodi and C. Kim, *npj Comput. Mater.*, 2017, **3**, 54.
12 A. Vriza, H. Chan and J. Xu, *Chem. Mater.*, 2023, **35**, 3046–3056.
13 Z. Zheng, O. Zhang, C. Borgs, J. T. Chayes and O. M. Yaghi, *J. Am. Chem. Soc.*, 2023, **145**, 18048–18062.
14 I. M. Pendleton, G. Cattabriga, Z. Li, M. A. Najeeb, S. A. Friedler, A. J. Norquist, E. M. Chan and J. Schrier, *MRS Commun.*, 2019, **9**, 846–859.
15 H. S. Stein, A. Sanin, F. Rahmanian, B. Zhang, M. Vogler, J. K. Flowers, L. Fischer, S. Fuchs, N. Choudhary and L. Schroeder, *Curr. Opin. Electrochem.*, 2022, **35**, 101053.
16 J. Amici, P. Asinari, E. Ayerbe, P. Barboux, P. Bayle-Guillemaud, R. J. Behm, M. Berecibar, E. Berg, A. Bhowmik, S. Bodoardo, *et al.*, *Adv. Energy Mater.*, 2022, **12**, 2102785.
17 C. Ling, *npj Comput. Mater.*, 2022, **8**, 33.
18 L. Su, M. Ferrandon, J. A. Kowalski, J. T. Vaughey and F. R. Brushett, *J. Electrochem. Soc.*, 2014, **161**, A1905.
19 S. Matsuda, K. Nishioka and S. Nakanishi, *Sci. Rep.*, 2019, **9**, 6211.
20 D. Martín-Yerga, M. Kang and P. R. Unwin, *ChemElectroChem*, 2021, **8**, 4240–4251.
21 S. Dieckhöfer, W. Schuhmann and E. Ventosa, *ChemElectroChem*, 2021, **8**, 3143–3149.
22 K. Sliozberg, D. Schäfer, T. Erichsen, R. Meyer, C. Khare, A. Ludwig and W. Schuhmann, *ChemSusChem*, 2015, **8**, 1270–1278.
23 C. Yada, C. E. Lee, D. Laughman, L. Hannah, H. Iba and B. E. Hayden, *J. Electrochem. Soc.*, 2015, **162**, A722.
24 D. Rajagopal, A. Koeppe, M. Esmaeilpour, M. Selzer, W. Wenzel, H. Stein and B. Nestler, *Adv. Energy Mater.*, 2023, **13**, 2301985.
25 S. G. Baird and T. D. Sparks, *Matter*, 2022, **5**, 4170–4178.
26 R. Pollice, G. dos Passos Gomes, M. Aldeghi, R. J. Hickman, M. Krenn, C. Lavigne, M. Lindner-D'Addario, A. Nigam, C. T. Ser, Z. Yao, *et al.*, *Acc. Chem. Res.*, 2021, **54**, 849–860.
27 I. E. Castelli, D. J. Arismendi-Arrieta, A. Bhowmik, I. Cekic-Laskovic, S. Clark, R. Dominko, E. Flores, J. Flowers, K. Ulvskov Frederiksen, J. Friis, *et al.*, *Batteries Supercaps*, 2021, **4**, 1803–1812.
28 M. Vogler, J. Busk, H. Hajiyani, P. B. Jørgensen, N. Safaei, I. E. Castelli, F. F. Ramirez, J. Carlsson, G. Pizzi, S. Clark, *et al.*, *Matter*, 2023, **6**, 2647–2665.
29 D. Guevarra, K. Kan, Y. Lai, R. J. Jones, L. Zhou, P. Donnelly, M. Richter, H. S. Stein and J. M. Gregoire, *Digital Discovery*, 2023, **2**, 1806–1812.
30 F. Rahmanian, J. Flowers, D. Guevarra, M. Richter, M. Fichtner, P. Donnely, J. M. Gregoire and H. S. Stein, *Adv. Mater. Interfaces*, 2022, **9**, 2101987.
31 P. Raghavan, B. C. Haas, M. E. Ruos, J. Schleinitz, A. G. Doyle, S. E. Reisman, M. S. Sigman and C. W. Coley, *ACS Cent. Sci.*, 2023, **9**, 2196–2204.
32 M. Krenn, R. Pollice, S. Y. Guo, M. Aldeghi, A. Cervera-Lierta, P. Friederich, G. dos Passos Gomes, F. Häse, A. Jinich, A. Nigam, *et al.*, *Nat. Rev. Phys.*, 2022, **4**, 1–9.
33 A. Benayad, D. Diddens, A. Heuer, A. N. Krishnamoorthy, M. Maiti, F. L. Cras, M. Legallais, F. Rahmanian, Y. Shin, H. Stein, *et al.*, *Adv. Energy Mater.*, 2022, **12**, 2102678.
34 F. Rahmanian, R. M. Lee, D. Linzner, K. Michel, L. Merker, B. B. Berkes, L. Nuss and H. S. Stein, *Attention towards chemistry agnostic and explainable battery lifetime prediction*, 2023.
35 L. Pascazio, S. Rihm, A. Naseri, S. Mosbach, J. Akroyd and M. Kraft, *J. Chem. Inf. Model.*, 2023, **21**, 6569–6586.
36 M. D. Wilkinson, M. Dumontier, I. J. Aalbersberg, G. Appleton, M. Axton, A. Baak, N. Blomberg, J.-W. Boiten, L. B. da Silva Santos, P. E. Bourne, *et al.*, *Sci. Data*, 2016, **3**, 1–9.
37 S. Rohrbach, M. Šiaučiulis, G. Chisholm, P.-A. Pirvan, M. Saleeb, S. H. M. Mehr, E. Trushina, A. I. Leonov, G. Keenan, A. Khan, *et al.*, *Science*, 2022, **377**, 172–180.
38 M. Christensen, L. P. Yunker, P. Shiri, T. Zepel, P. L. Prieto, S. Grunert, F. Bork and J. E. Hein, *Chem. Sci.*, 2021, **12**, 15473–15490.
39 P. Shiri, V. Lai, T. Zepel, D. Griffin, J. Reifman, S. Clark, S. Grunert, L. P. Yunker, S. Steiner, H. Situ, *et al.*, *Iscience*, 2021, **24**, 102176.
40 S. Eppel, H. Xu, M. Bismuth and A. Aspuru-Guzik, *ACS Cent. Sci.*, 2020, **6**, 1743–1752.
41 G. Smith and E. J. Dickinson, *Nat. Commun.*, 2022, **13**, 6832.

42 S. Daboss, F. Rahmanian, H. S. Stein and C. Kranz, *Electrochem. Sci. Adv.*, 2022, **2**, e2100122.

43 B. Burger, P. M. Maffettone, V. V. Gusev, C. M. Aitchison, Y. Bai, X. Wang, X. Li, B. M. Alston, B. Li, R. Clowes, *et al.*, *Nature*, 2020, **583**, 237–241.

44 F. Rahmanian, *Auto-MISCHBARES*, 2023, **https://github.com/fuzhanrahmanian/MISCHBARES**.

45 Bokeh Development Team, *Bokeh: Python library for interactive visualization*, 2018.

46 S. Back, A. Aspuru-Guzik, M. Ceriotti, G. Gryn'ova, B. A. Grzybowski, G. H. Gu, J. E. Hein, K. Hippalgaonkar, R. Hormazabal, Y. Jung, *et al.*, *Digital Discovery*, 2024, **3**(1), 22–33.

47 P. M. Maffettone, P. Friederich, S. G. Baird, B. Blaiszik, K. A. Brown, S. I. Campbell, O. A. Cohen, R. L. Davis, I. T. Foster, N. Haghmoradi, *et al.*, *Digital Discovery*, 2023, **2**, 1644–1659.

48 M. Grinberg, *Flask web development: developing web applications with python*, O'Reilly Media, Inc., 2018.

49 G. Bradski, *Dr. Dobb's Journal of Software Tools*, 2000.

50 F. Rahmanian, *Auto-MISCHBARES: Tutorial & Demonstration*, 2023, DOI: **10.5281/zenodo.10445749**.

51 F. Rahmanian, *Modular and Autonomous Data Analysis Platform (MADAP)*, 2023, DOI: **10.5281/zenodo.10357192**.

52 C. Draxl and M. Scheffler, *J. Phys.: Mater.*, 2019, **2**, 036001.

53 M. Uhrin, S. P. Huber, J. Yu, N. Marzari and G. Pizzi, *Comput. Mater. Sci.*, 2021, **187**, 110086.

54 J. Medina, A. W. Ziaullah, H. Park, I. E. Castelli, A. Shaon, H. Bensmail and F. El-Mellouhi, *Matter*, 2022, **5**, 3614–3642.

55 T. Haerder and A. Reuter, *ACM computing surveys (CSUR)*, 1983, 15, 287–317.

56 S. P. Kühn, K. Edström, M. Winter and I. Cekic-Laskovic, *Adv. Mater. Interfaces*, 2022, **9**, 2102078.

57 H. Wang, X. Li, F. Li, X. Liu, S. Yang and J. Ma, *Electrochem. Commun.*, 2021, **122**, 106870.

58 X. Chen, W. Shen, T. T. Vo, Z. Cao and A. Kapoor, *2012 10th International Power & Energy Conference (IPEC)*, 2012, pp. 230–235.

59 D. Anseán González, M. González Vega, J. C. Viera Pérez, J. C. Álvarez Álvarez, C. J. Blanco Viejo, V. García *et al.*, *Conference and Exhibition-2013 International Conference on New Concepts in Smart Cities: Fostering Public and Private Alliances, SmartMILE 2013*, 2013.

60 P. Ayuso, H. Beltran, J. Segarra-Tamarit and E. Pérez, *Math. Comput. Simulat.*, 2021, **183**, 97–115.

61 N. Fairley, V. Fernandez, M. Richard-Plouet, C. Guillot-Deudon, J. Walton, E. Smith, D. Flahaut, M. Greiner, M. Biesinger, S. Tougaard, *et al.*, *Appl. Surf. Sci. Adv.*, 2021, **5**, 100112.

62 M. Mao, B. Huang, Q. Li, C. Wang, Y.-B. He and F. Kang, *Nano Energy*, 2020, **78**, 105282.

63 Y. Pan, G. Wang and B. L. Lucht, *Electrochim. Acta*, 2016, **217**, 269–273.

64 J. Ming, M. Li, P. Kumar and L.-J. Li, *ACS Nano*, 2016, **10**, 6037–6044.

65 Z.-Y. Chen, H.-L. Zhu, Z. Wei, J.-L. Zhang and Q.-F. Li, *Trans. Nonferrous Met. Soc. China*, 2010, **20**, 614–618.

66 J. Hou, R. Girod, N. Nianias, T.-H. Shen, J. Fan and V. Tileli, *J. Electrochem. Soc.*, 2020, **167**, 110515.

67 L. T. N. Huynh, H. H. A. Nguyen, T. T. D. Tran, T. T. T. Nguyen, T. M. A. Nguyen, T. H. La, V. M. Tran, M. L. P. Le, *et al.*, *J. Nanomater.*, 2019, **2019**, 2464920.

68 N. Elgrishi, K. J. Rountree, B. D. McCarthy, E. S. Rountree, T. T. Eisenhart and J. L. Dempsey, *J. Chem. Educ.*, 2018, **95**, 197–206.

69 N. Mahne, S. E. Renfrew, B. D. McCloskey and S. A. Freunberger, *Angew. Chem., Int. Ed.*, 2018, **57**, 5529–5533.

70 R. Wang, X. Yu, J. Bai, H. Li, X. Huang, L. Chen and X. Yang, *J. Power Sources*, 2012, **218**, 113–118.

71 K. Tasaki, A. Goldberg, J.-J. Lian, M. Walker, A. Timmons and S. J. Harris, *J. Electrochem. Soc.*, 2009, **156**, A1019.

72 Z.-W. Yin, X.-X. Peng, J.-T. Li, C.-H. Shen, Y.-P. Deng, Z.-G. Wu, T. Zhang, Q.-B. Zhang, Y.-X. Mo, K. Wang, *et al.*, *ACS Appl. Mater. Interfaces*, 2019, **11**, 16214–16222.

73 Q. Li, Y. Wang, X. Wang, X. Sun, J.-N. Zhang, X. Yu and H. Li, *ACS Appl. Mater. Interfaces*, 2019, **12**, 2319–2326.

74 F. Häse, L. M. Roch and A. Aspuru-Guzik, *Chem. Sci.*, 2018, **9**, 7642–7655.

75 F. Häse, M. Aldeghi, R. J. Hickman, L. M. Roch and A. Aspuru-Guzik, *Applied Physics Reviews*, 2021, **8**, 031406.